Photoelectron Angular Distributions and Cross Section Ratios of Two-Color Two-Photon Above Threshold Ionization of Argon†

Louis H. Haber, Benjamin Doughty, and Stephen R. Leone*

Departments of Chemistry and Physics and Lawrence Berkeley National Laboratory, University of California, Berkeley, California 94720

Received: April 8, 2009; Revised Manuscript Received: June 26, 2009

Anisotropy parameters and cross section ratios of two-color two-photon above threshold ionization sidebands from argon are measured using photoelectron velocity map imaging with the selected 13th or 15th high-order harmonics in a perturbative 800 nm dressing field. A new data analysis technique determines accurate anisotropy parameters of the photoelectron angular distributions for each sideband by subtracting a sequence of percentages of the single-photon ionization background from the above threshold ionization signal to correct for the angular averaging of overlapping photoelectron energies. The results provide a fundamental test of theoretical predictions based on second-order perturbation theory with a one-electron model and the soft-photon approximation and show agreement with theory for the cross section ratios. However, discrepancies between the theoretically predicted and experimentally determined photoelectron angular distributions demonstrate the need for a more comprehensive theoretical description of two-color two-photon above threshold ionization.

Introduction

The interaction of intense, ultrashort pulses of 800 nm light with atoms allows for the detailed study of processes such as the generation of high-order harmonics[1] (HH) and above threshold ionization[2] (ATI). High-order harmonics provide extreme ultraviolet (EUV) photons with temporal pulse widths ranging from picoseconds to attoseconds that are useful for time-resolved pump−probe experiments on atoms and molecules.[1] Above threshold ionization occurs when an atom or molecule absorbs more photons than are needed for ionization, and this process is well characterized for monochromatic light.[2,3] When high-order harmonics with sufficient energy for single-photon ionization (SPI) are spatially overlapped with an intense infrared (IR) dressing field, the photoelectron spectrum displays positive and negative sidebands corresponding to the simultaneous absorption of an EUV photon with the absorption and emission of an additional IR photon, respectively, in a process identified as two-color two-photon above threshold ionization.[1]

Two-color two-photon above threshold ionization has been the subject of many recent experimental studies.[4−8] Detection of photoelectron angular distributions of mixed-color two-photon ATI sidebands allows for the characterization of attosecond pulse trains through interferences between pathways involving adjacent high-order harmonics.[4−7] By scanning the time delay between the EUV comb of the high-order harmonics and the IR light, the relative phases between neighboring harmonics can be determined enabling temporal reconstruction of the EUV pulses.[4] Additional studies measure the sideband intensities as a function of the relative angle between the EUV and IR polarizations.[8] These mixed-color experimental results are dominated by effects from multiple EUV harmonic energies, obscuring the cross-sectional and angular ATI information originating from a single EUV energy alone. Recently, using a monochromatic EUV free-electron laser combined with an intense optical laser in helium, the ATI sideband intensities are measured as a function of the relative angle between polarization vectors, allowing for the ratios of *s* to *d* character of the sideband photoelectrons to be determined.[9] With change in the intensity of the optical dressing field, the lower-intensity perturbative and higher-intensity nonperturbative regimes are observed,[9] in agreement with theoretical expectations.[10] However, photoelectron angular distributions (PADs) from individual ATI sidebands arising from energy-selected EUV pulses interacting with an optical dressing field have not been characterized experimentally.

Photoelectron angular distributions are the result of interferences between different quantum pathways of photoionization.[11] The outgoing photoelectrons are composed of separate partial waves, each with different angular momenta, intensities, and phase shifts. Measurements of PADs from resonant two-photon ionizations of atoms have yielded complete information on the photoionization of bound states for a few cases.[12−17] Similar measurements of energy-selected two-color two-photon above threshold ionization will allow for a detailed study of atomic free−free transitions, enabling a more sensitive test for theoretical descriptions than cross section measurements alone.

In this paper, we use velocity map imaging to measure the cross section ratios between positive and negative ATI sidebands as well as the photoelectron angular distributions of each individual sideband that result from the combination of either the selected 13th or 15th high-order harmonic with a perturbative 800 nm dressing field in atomic argon. The cross section ratios are in excellent agreement with calculations that use second-order perturbation theory[18] (SOPT) and a one-electron model.[13,19,20] Additional theoretical predictions using the soft-photon approximation[21,22] (SPA) reproduce the cross section ratio for the 15th HH sidebands but result in inaccuracies for the sidebands of the lower-energy 13th HH. Finally, significant discrepancies between the experimentally determined and theoretically derived anisotropy parameters are observed, demonstrating the need for

† Part of the "Robert W. Field Festschrift".

10.1021/jp903231n CCC: $40.75
Published on Web 07/17/2009

more sophisticated theoretical treatments of two-color two-photon above threshold ionization of the 3*p* electron of argon.

Experimental Setup

The experimental setup is described in a previous study.[12] Briefly, the output of an amplified Ti:sapphire laser system producing 50 fs, 2.4 mJ pulses centered at 800 nm with a 1 kHz repetition rate is sent to a 50:50 beam splitter to create two beams. The first beam is focused into a pulsed jet of argon to generate high-order harmonics. Either the 13th or 15th high-order harmonic is selected and focused to a separate skimmed effusive atomic beam of argon at the interaction region using a home-built EUV monochromator. The second 800 nm beam is sent to a retroreflector on a delay stage to control the temporal pulse delay before being focused to the interaction region to overlap with the EUV beam at a relative angle of ~1.5°. Photon intensities of $\sim 5 \times 10^{10}$ and $\sim 1 \times 10^4$ W/cm^2 are estimated for the IR and EUV foci, respectively. A velocity map imaging[23] (VMI) electrostatic lens projects the resulting three-dimensional sphere of expanding photoelectrons onto a two-dimensional position-sensitive detector connected to a computer. Half-wave plates control the directions of the electric vectors of the linearly polarized EUV and IR pulses to be collinear and parallel to the detector face. A beam-block opens and shuts the IR pulse in synchronization with an automatic file saving program to record EUV-only background images and EUV+IR signal images at 1 min intervals over ~1 day of data acquisition for each EUV photon energy.

The experimental conditions are carefully chosen to study fundamental properties of two-color two-photon above threshold ionization while avoiding extreme limits of photon field strengths or pulse widths where a two-photon description is insufficient. The IR intensities are controlled to be in the perturbative regime,[10] so that additional ATI sidebands are minimized and so that the resulting cross section ratios between the positive and negative ATI sidebands and the PADs of each individual sideband are independent of the photon intensities. The signals of the ATI sidebands and the depletion of the SPI by the dressing field follow a Gaussian form as a function of the time delay between the EUV and IR pulses, with a full width half-maximum of approximately 100 fs, given by the temporal resolution of the experiment. The diffraction grating of the EUV monochromator temporally broadens the high-order harmonic pulses so that momentum shifts[7,24] associated with attosecond pulse trains in strong fields are not observed. As a result, there is no change in either the cross section ratios or the photoelectron angular distributions as a function of EUV-IR temporal pulse delay, to within experimental uncertainty.

Analysis and Results

Measurements of the cross section ratios and photoelectron angular distributions of the positive and negative sidebands allow for a fundamental study of two-color two-photon above threshold ionization. The ATI signals energetically overlap with a much larger background from the single-photon ionization, making data analysis difficult. In the EUV+IR image, the overall ATI signal is ~2% of the overall single-

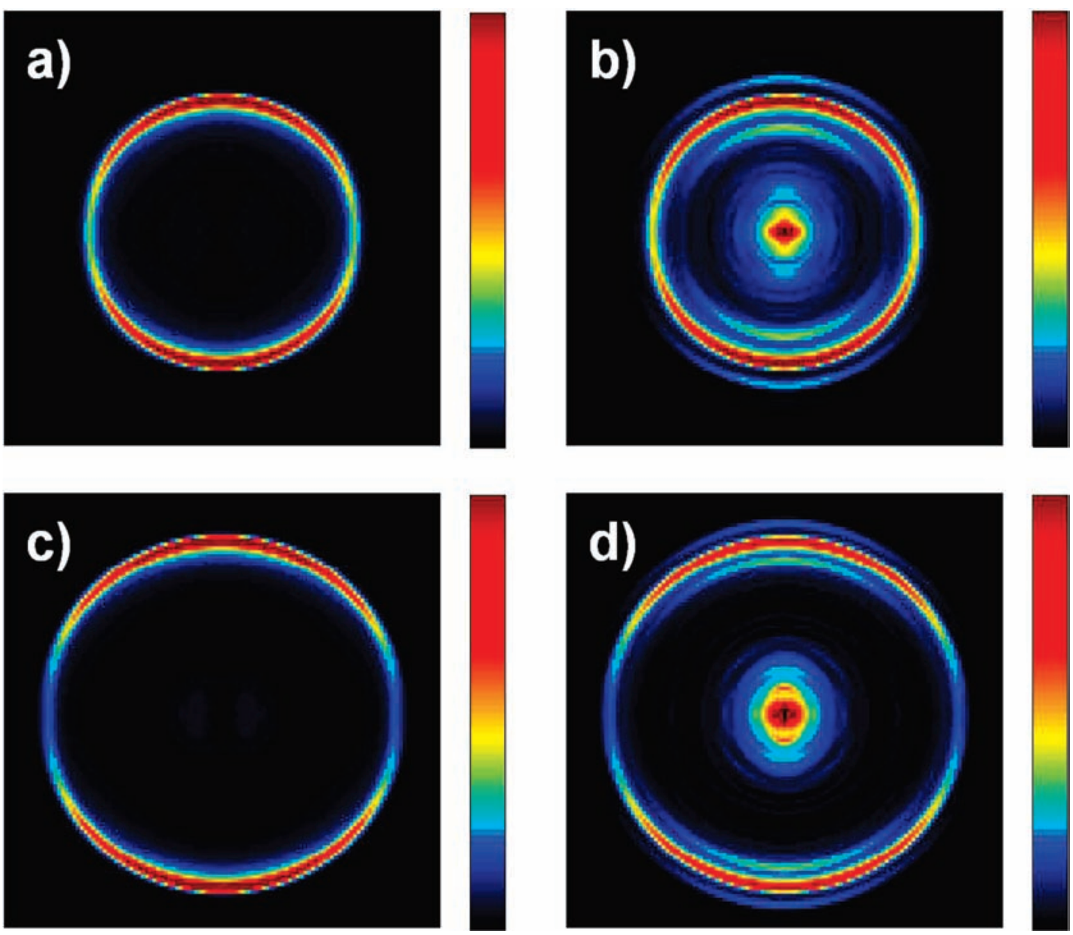

Figure 1. Inverted photoelectron images of Ar from (a) the 13th HH, (b) the 13th HH + 800 nm using 85% background subtraction, (c) the 15th HH, and (d) the 15th HH + 800 nm using 85% background subtraction.

photon ionization background and there is ~2% depletion of the SPI signal, resulting in approximately the same number of counts for each EUV+IR and EUV-only image. Photoelectrons from SPI and ATI spatially overlap on the velocity map image, although the corresponding peaks reach maxima at different radii from the image center. Subtracting the background images from the signal images results in negative intensities near the SPI radial peaks and positive intensities near the ATI radial peaks. Novel data analysis techniques are developed to extract all relevant information from the background and signal images in order to accurately characterize the cross sections and photoelectron angular distributions of the ATI measurements.

Because the directions of the linear polarizations of the EUV and IR photons are collinear, the angular distributions of the two-photon ATI photoelectrons are given by

$$I(\theta) = \frac{\sigma}{4\pi}[1 + \beta_2 P_2(\cos\theta) + \beta_4 P_4(\cos\theta)] \qquad (1)$$

where σ is the total cross section, θ is the angle between the laser polarization and the electron velocity vectors, and β_2 and β_4 are the anisotropy parameters associated with the second- and fourth-order Legendre polynomials, respectively.[11] This contrasts with single-photon ionization, where $\beta_4 = 0$ and $-1 \leq \beta_2 \leq 2$.[19] The pBASEX[25] program inverts the photoelectron images using the second- and fourth-order Legendre polynomials to recover the energies and angular distributions of the photoelectrons; however, inaccuracies result when the images contain significant negative values. A method is constructed here whereby a series of percentages of the EUV-only background images ranging from 0 to 100% is subtracted from the EUV+IR signal images, and these background-subtracted images are each inverted separately for more detailed analysis. The background-subtracted EUV+IR images are then renormalized to correctly account for the depletion of the SPI peak.

Subtracting a percentage of the background preferentially enhances the ATI signal with respect to the SPI background. The inverted images of EUV-only backgrounds and the EUV+IR signals using 85% background subtraction from the selected 13th and 15th high-order harmonics are shown in Figure 1, which clearly displays the SPI and ATI rings. Using a background subtraction of 85% increases the relative amplitudes of the ATI sidebands to a maximum amount while still avoiding negative intensities in the background-subtracted image so that the cross section ratios and PADs have the best accuracies, as demonstrated later in this paper. The electric vectors of the linearly polarized EUV and IR photons are directed vertically in each image. Intensities in the center of the EUV+IR inverted images are from multiphoton ionization of background gases by the IR pulses and do not affect the results. The pBASEX inversion program also yields the fitted anisotropy parameters, β_2 and β_4, as well as the signal intensity as a function of the inverted image radius. The radius of each inverted image is directly proportional to the photoelectron speed, allowing for the determination of the photoelectron energy spectrum. Figure 2a shows the photoelectron energy spectra resulting from the inverted images of panels a and b of Figure 1 for the 13th HH, while Figure 2b shows the differences between these spectra. Similarly, Figure 3a shows the photoelectron energy spectra resulting from the inverted images of panels c and d of Figure 1 for the 15th HH, while Figure 3b shows the difference between these spectra.

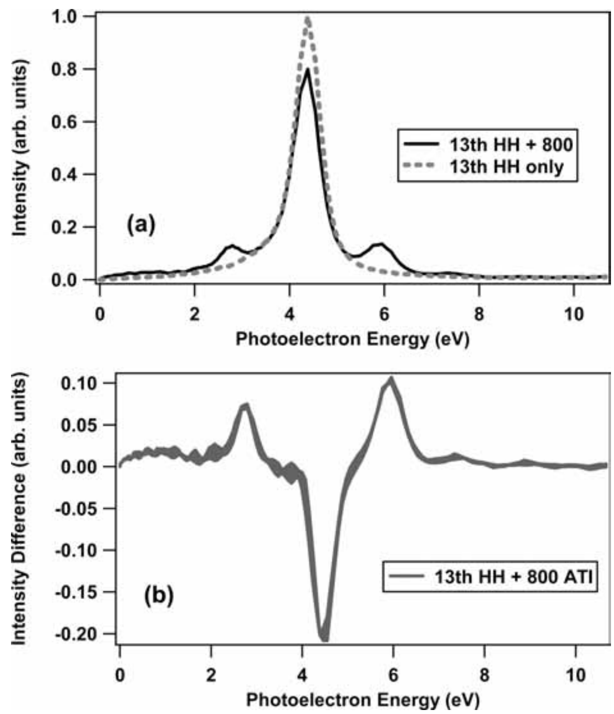

Figure 2. (a) Photoelectron energy spectra of Ar from the 13th HH and the 13th HH + 800 nm using 85% background subtraction. (b) The difference between these photoelectron spectra, where the line width represents the uncertainty of the intensity at each energy.

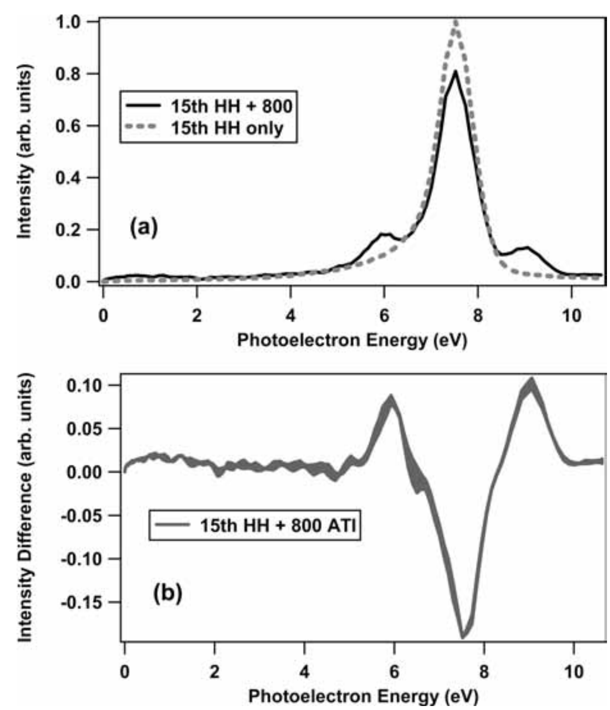

Figure 3. (a) Photoelectron energy spectra of Ar from the 15th HH and the 15th HH + 800 nm using 85% background subtraction. (b) The difference between these photoelectron spectra, where the line width represents the uncertainty of the intensity at each energy.

The photoelectron spectra clearly show the positive and negative ATI sidebands that occur at one photon energy above and below the depleted SPI peaks, respectively. The single-photon ionization of argon by the 13th harmonic results in photoelectrons peaked at 4.30 ± 0.08 eV with a full width half-maximum of 0.65 eV. The single-photon ionization of argon by the 15th harmonic results in photoelectrons peaked at 7.42

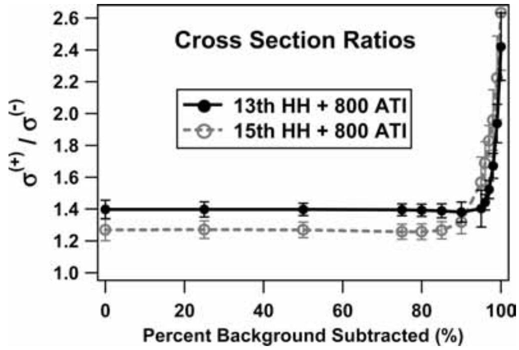

Figure 4. The ratios of the cross sections between the positive and negative ATI sidebands of the 13th HH + 800 nm and the 15th HH + 800 nm as a function of percent background subtracted.

± 0.10 eV with a full width half-maximum of 0.91 eV. The full width half-maxima of the SPI peaks, due mostly to the bandwidths of the EUV pulses, are larger than the 0.18 eV spin−orbit splitting of the argon ion, preventing resolution of the separate $P_{3/2}$ and $P_{1/2}$ ion states. The SPI photoelectron spectra are consistent with photon energies of 20.1 and 23.2 eV for the 13th and 15th harmonics, respectively. The positive and negative ATI sidebands of the 13th harmonic have peaks centered at 5.86 ± 0.09 and 2.73 ± 0.06 eV, respectively, with full width half-maxima of 0.68 and 0.49 eV, respectively. The positive and negative ATI sidebands of the 15th harmonic have peaks centered at 8.95 ± 0.11 and 5.84 ± 0.09 eV, respectively, with full width half-maxima of 0.84 and 0.64 eV, respectively. The energy separations between SPI and ATI peaks are all equal to one photon energy of 800 nm and no ponderomotive energy shifts are observed, to within experimental energy resolution.

The measured cross section ratios between the positive and negative ATI sidebands are determined by summing the intensities of the difference spectra over the full width half-maximum of the radial distribution for each sideband peak. Because the positive EUV+IR and negative EUV−IR sidebands are produced concurrently under the same experimental conditions and photon fluxes, the ratio of the areas of the full width half-maximum peaks is equal to the ratio of the cross sections. The measured cross section ratios of the ATI sidebands are plotted as a function of percent background subtracted in Figure 4. Superscripts (+) or (−) indicate measurements corresponding to the positive EUV+IR or the negative EUV−IR sideband, respectively. These values are shown to be constant over a broad range of background subtraction percentages, up to about 90% when negative values in the images cause inaccuracies in the inversions. The cross section ratios of the ATI sidebands using 85% background subtraction, as depicted for Figures 1−3, are 1.39 ± 0.04 and 1.27 ± 0.05 for the 13th and 15th high-order harmonics, respectively, and these values are listed in Table 1.

The anisotropy parameters associated with the photoelectron angular distributions are sensitive measurements of the detailed interactions between the two photons with the atom and the resulting ion and photoelectron. The anisotropy parameters are experimentally determined by a weighted average over the full width half-maximum of the radial distribution of each photoelectron peak, given by $\beta_i = \sum I\beta_i(r)/\sum I$, where I is the intensity and $\beta_i(r)$ is the anisotropy parameter as a function of the inverted image radius. The anisotropy parameters associated with an unconstrained fit to the second- and fourth-order Legendre polynomials from the single-photon ionization of argon are obtained to be 0.86 ± 0.01 and 0.00 ± 0.01, respectively, for the 13th HH, and 1.32 ± 0.01 and 0.00 ± 0.01, respectively,

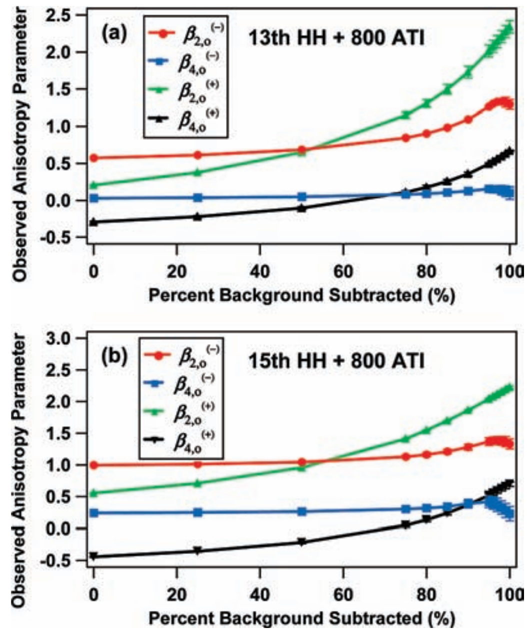

Figure 5. The experimentally observed anisotropy parameters of the positive and negative ATI sidebands for (a) the 13th HH + 800 nm and (b) the 15th HH + 800 nm as a function of percent background subtracted.

for the 15th HH. These values are in excellent agreement with literature values[26,27] and are consistent with the expectations that $\beta_4 = 0$ for SPI, validating the high accuracy of the velocity map imaging setup and analysis.

The anisotropy parameters of the ATI sidebands are more difficult to determine due to their relatively weak signal and partial overlap with the SPI background. ATI photoelectrons that energetically overlap with the SPI background in the inverted image result in an averaging of anisotropy parameters given by the equation, $\beta_{i,o} = R_b\beta_{i,b} + R_s\beta_{i,s}$, where $\beta_{i,o}$ is the empirically observed anisotropy parameter of the ATI peak, $\beta_{i,b}$ is the anisotropy parameter of the background at the ATI peak energy, R_b and R_s are the relative intensities of the background and ATI signal such that $R_b + R_s = 1$, and $\beta_{i,s}$ is the correct anisotropy parameter of the ATI signal of interest. By changing the percentage of the EUV-only background that is subtracted from the EUV+IR signal, the relative intensities of R_b and R_s change, allowing for an accurate determination of $\beta_{i,s}$. The observed anisotropy parameters of the ATI sidebands for the 13th and 15th high-order harmonics are plotted as a function of percent background subtracted in panels a and b of Figure 5, respectively. The anisotropy parameters from background SPI for the negative and positive sidebands of the 13th HH are $\beta_{2,b}^{(-)} = 0.43 \pm 0.01$, $\beta_{4,b}^{(-)} = 0.00 \pm 0.01$, $\beta_{2,b}^{(+)} = -0.55 \pm 0.01$, and $\beta_{4,b}^{(+)} = -0.62 \pm 0.01$, respectively. The anisotropy parameters from background SPI for the negative and positive sidebands of the 15th HH are $\beta_{2,b}^{(-)} = 0.93 \pm 0.02$, $\beta_{4,b}^{(-)} = 0.21 \pm 0.01$, $\beta_{2,b}^{(+)} = -0.14 \pm 0.01$, and $\beta_{4,b}^{(+)} = -0.83 \pm 0.01$, respectively. The anisotropy parameters at the edges of the SPI peaks result from small deviations from ideal velocity map imaging configurations.

The corrected anisotropy parameters of the ATI sidebands from the 13th HH ± 800 nm and the 15th HH ± 800 nm are plotted as a function of percent background subtracted in parts a and b of Figure 6, respectively. These values are shown to be constant over a broad range of background subtraction percentages, up to about 90% where negative values in the images start to cause inaccuracies in the inversions. The corrected anisotropy

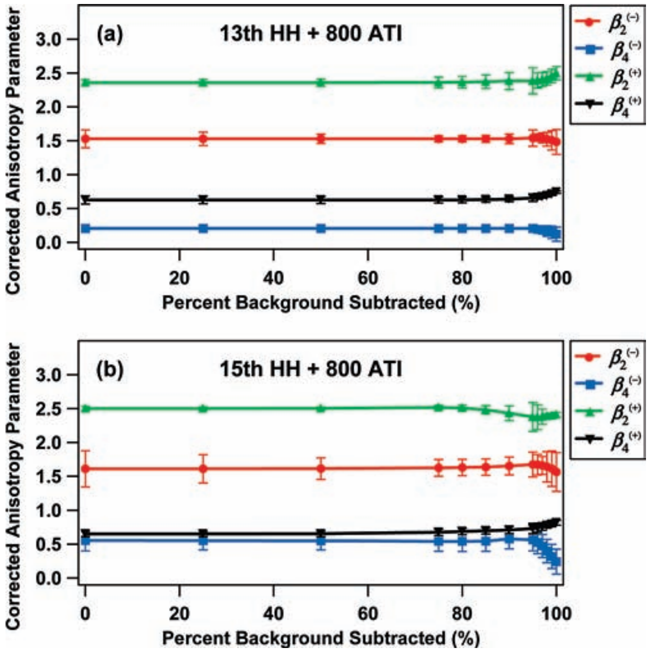

Figure 6. The corrected anisotropy parameters of the positive and negative ATI sidebands for (a) the 13th HH + 800 nm and (b) the 15th HH + 800 nm as a function of percent background subtracted.

parameters of the ATI sidebands using 85% background subtraction, as depicted for Figures 1−3, are $\beta_2^{(-)} = 1.52 \pm 0.05$, $\beta_4^{(-)} = 0.21 \pm 0.05$, $\beta_2^{(+)} = 2.37 \pm 0.10$, and $\beta_4^{(+)} = 0.63 \pm 0.04$ for 13th HH ± 800 nm, and are $\beta_2^{(-)} = 1.63 \pm 0.12$, $\beta_4^{(-)} = 0.54 \pm 0.15$, $\beta_2^{(+)} = 2.48 \pm 0.06$, and $\beta_4^{(+)} = 0.69 \pm 0.05$ for 15th HH ± 800 nm. These results are listed in Table 1.

Discussion

The experimentally determined cross section ratios and photoelectron angular distributions of the two-color two-photon ATI sidebands can be directly compared to theoretical predictions that use either second-order perturbation theory[18] or the soft-photon approximation.[21] With second-order perturbation theory, the two-photon matrix elements are determined to be complex, with the real part corresponding to the principle-value integration over the continuum and the imaginary part corresponding to a simple product of two single-photon matrix elements.[18] In the low-intensity limit, the cross section of the ATI sideband is expressed as $\sigma = \sum_{if}|F_1F_2\tilde{M}_{if}|^2$, where F_1 and F_2 are the electric fields of the EUV and IR photons, respectively, and $\tilde{M}_{if}$ is the complex two-photon matrix element between the initial state i and the final state f. The ratios of the cross sections between different ATI sidebands can be expressed as

$$\sigma^{(+)}/\sigma^{(-)} = \sum_{if} |\tilde{M}_{if}^{(+)}|^2 / \sum_{if'} |\tilde{M}_{if'}^{(-)}|^2 \qquad (2)$$

which is independent of photon field strengths. Using the $\tilde{M}_{if}$ values tabulated using SOPT,[18] the theoretically predicted cross section ratios, $\sigma^{(+)}/\sigma^{(-)}$, for ATI sidebands from 13th HH + 800 nm and 15th HH + 800 nm are 1.42 and 1.28, respectively. These values are in excellent agreement with our experimentally measured cross section ratios, as shown in Table 1.

The anisotropy parameters for the ATI sidebands can be predicted by second-order perturbation theory using the expression for the photoelectron angular distributions

$$I(\theta,\phi) = (F_1F_2)^2 \sum_i |\sum_f \tilde{M}_{if} Y_{l_f m_f}(\theta,\phi) e^{i\delta_{l_f}}|^2 \qquad (3)$$

where $Y_{l_f m_f}(\theta,\phi)$ are spherical harmonics that depend on the angles, θ and ϕ, between the laser polarization and electron velocity vectors, l_f and m_f are the angular momentum and magnetic quantum numbers of the final state f, and δ_{l_f} is the phase shift of the outgoing partial wave.[18] Because the $3p$ electron of the initial state i is unaligned and all transitions are constrained by the selection rules for linearly polarized light ($\Delta l = \pm 1$, $\Delta m = 0$), the photoelectron angular distribution of each two-photon ATI sideband can be expressed by eq 1, as expected, characterized exclusively by anisotropy parameters associated with the second- and fourth order Legendre polynomials. The sideband photoelectrons are composed of partial waves of p and f symmetry with $m = 0, +1$, or -1. Anisotropy parameters associated with the sixth-order Legendre polynomial that are possible from f wave symmetry are all equal to zero because the initial p electron is unaligned. The sideband PADs depend on the partial wave intensities from the two-photon transition matrices, as well as the phase shift differences between the p and f waves. Use of the tabulated values[18] of $\tilde{M}_{if}$ and δ_{l_f} results in predicted anisotropy parameters of $\beta_2^{(-)} = 1.97$, $\beta_4^{(-)} = 0.40$, $\beta_2^{(+)} = 1.68$, and $\beta_4^{(+)} = 0.54$ for the ATI sidebands of the 13th HH ± 800 nm, and $\beta_2^{(-)} = 1.63$, $\beta_4^{(-)} = 0.40$, $\beta_2^{(+)} = 1.28$, and $\beta_4^{(+)} = 0.45$ for the ATI sidebands of the 15th HH ± 800 nm. Except for the fortuitous agreement with the negative 15th HH − 800 nm sideband, these theoretically predicted anisotropy parameters are not in agreement with the experimental measurements, as shown in Table 1. Adjusting only the phase shift differences cannot correct for the discrepancies in the theoretically derived PADs of the ATI sidebands.

Deviations between the theoretically predicted photoelectron angular distributions of the ATI sidebands using second-order perturbation theory and the experimentally determined results can be attributed to many reasons. PADs are a more sensitive test than cross sections because they result from complicated interferences between different quantum pathways and because they depend critically on the phase shifts and two-photon matrix elements of the outgoing partial waves. In addition, this theoretical treatment uses the one-electron model, which has many underlying assumptions that work well for small atoms[12,14,15] like H^-, He, and Li, but lead to inaccuracies for larger atoms[16,17] (Ar, Rb). The one-electron model describes photoionization as a process of a single electron interacting in a spherically symmetric, screened Coulomb field with no electron−electron correlations.[20] However, careful inspection of the theory shows that the expected ATI partial cross sections are larger for the Ar $3p_z$ electrons than for the $3p_x$ or $3p_y$ electrons at these photon energies.[18] For example, the theoretically predicted partial cross section ratios are $\sigma_{p_z}^{(+)}/\sigma_{p_{x,y}}^{(+)} = 2.19$ and $\sigma_{p_z}^{(-)}/\sigma_{p_{x,y}}^{(-)} = 2.62$ for the 13th HH ± 800 nm ATI sidebands, and are $\sigma_{p_z}^{(+)}/\sigma_{p_{x,y}}^{(+)} = 2.57$ and $\sigma_{p_z}^{(-)}/\sigma_{p_{x,y}}^{(-)} = 2.99$ for the 15th HH ± 800 nm ATI sidebands. This results in final potentials that are not spherically symmetric, in violation of the one-electron model's description. In addition, the model potential used in the theoretical calculation completely neglects spin−orbit coupling that results in the different $^2P_{1/2}$ and $^2P_{3/2}$ ion states, where the $M_J = \pm 1/2$ states are each equally populated in $^2P_{1/2}$ but the $M_J = \pm 1/2$ and the $M_J = \pm 3/2$ states in $^2P_{3/2}$ can have different populations. Finally,

TABLE 1: The Experimentally Determined Cross Section Ratios and Anisotropy Parameters of the ATI Sidebands Compared to Theoretical Predictions[a]

	$\sigma^{(+)}/\sigma^{(-)}$	$\beta_2^{(-)}$	$\beta_4^{(-)}$	$\beta_2^{(+)}$	$\beta_4^{(+)}$
13th HH + 800 nm experiment	1.39 ± 0.04	1.52 ± 0.05	0.21 ± 0.05	2.37 ± 0.10	0.63 ± 0.04
13th HH + 800 nm theory: SOPT	1.42	1.97	0.40	1.68	0.54
13th HH + 800 nm theory: SPA	1.78	2.27	0.35	2.59	0.79
15th HH + 800 nm experiment	1.27 ± 0.05	1.63 ± 0.12	0.54 ± 0.15	2.48 ± 0.06	0.69 ± 0.05
15th HH + 800 nm theory: SOPT	1.28	1.69	0.40	1.28	0.45
15th HH + 800 nm theory: SPA	1.27	2.59	0.79	2.69	0.92

[a] Superscripts (+) or (−) indicate sidebands corresponding to positive EUV+IR or negative EUV−IR sidebands, respectively.

electron−electron correlation effects probably cannot be neglected in the many-electron argon atom, providing a possible reason for additional deviations. Although this model proves very successful for cross section ratios, it does not successfully reproduce the photoelectron angular distributions.

An alternate theoretical approach to describe two-color two-photon above threshold ionization uses the soft-photon approximation in the low field limit. The soft-photon approximation describes the scattering of a free electron off an atomic potential in the presence of a low-frequency optical field and is expected to give accurate results as long as the kinetic energy of the photoelectron is at least ∼15 times larger than the dressing field photon energy.[10,21] Although this condition is not satisfied under our experiment, it is instructive to compare theoretical predictions for the photoelectron angular distributions and the cross section ratios using the soft-photon approximation to those from second-order perturbation theory and to our experimental results.

The photoelectron angular distributions of a two-color above threshold ionization under the soft-photon approximation is given by

$$\left(\frac{d\sigma^{(n)}}{d\theta}\right)_{E_k} = \frac{k}{k_0} J_n^{\,2}(\boldsymbol{\alpha_0}\cdot\boldsymbol{K})\left(\frac{d\sigma^{(0)}}{d\theta}\right)_{E_k} \qquad (4)$$

where n describes the number of low-energy photons exchanged ($n < 0$ for absorption and $n > 0$ for stimulated emission, resulting in the positive and negative sidebands, respectively) after the absorption of one high-energy photon.[21] The differential cross section from single photon ionization is $d\sigma^{(0)}/d\theta$, given at the final kinetic energy of E_k. The dressing field acts on the scattering electron by the Bessel function, $J_n(z)$, where $\boldsymbol{\alpha_0} = \boldsymbol{F_{0L}}/\omega_L^2$ is the classical excursion vector of a free electron in a laser field with amplitude F_{0L} and frequency ω_L, and $\boldsymbol{K} = \boldsymbol{k} - \boldsymbol{k_0}$ is the electron's momentum transfer from its initial incoming wave vector $\boldsymbol{k_0}$ to its final state wave vector $\boldsymbol{k}$, all in atomic units.

The soft-photon approximation does not include the two-photon matrix elements or the phase shift differences of the final partial waves but instead views the outgoing electron semiclassically. In the low-intensity limit, $n = \pm 1$ ATI sidebands dominate and $\alpha_0 K$ is much less than 1, so the squared Bessel functions $J^2_{\pm 1}(z)$ are proportional to $\cos^2 \theta$ and the sideband photoelectron angular distributions, given by eq 1, are determined only by the single-photon anisotropy parameter, $\beta_2^{(0)}$, at the final kinetic energy E_k. Taking the experimentally measured single-photon ionization PADs[26] where $\beta_2^{(0)}$ is equal to approximately 0.4, 1.1, and 1.4 for photoelectron energies of 2.7, 5.8, and 9.0 eV, respectively, corresponding to the energies of the ATI sidebands of interest, and $\beta_4^{(0)}$ is equal to zero for all SPI photoelectrons, as expected, the theoretically predicted anisotropy parameters are $\beta_2^{(-)} = 2.27$, $\beta_4^{(-)} = 0.35$, $\beta_2^{(+)} = 2.59$, $\beta_4^{(+)} = 0.79$ for the negative and positive sidebands of the 13th HH, respectively, and are $\beta_2^{(-)} = 2.59$, $\beta_4^{(-)} = 0.79$, $\beta_2^{(+)} = 2.69$, $\beta_4^{(+)} = 0.92$ for the negative and positive sidebands of the 15th HH, respectively. Notice that the anisotropy parameters that are theoretically predicted using the SPA are equal for the positive sideband of the 13th HH and the negative sideband of the 15th HH because the final energies are the same. As shown in Table 1, these theoretically predicted anisotropy parameters do not agree with the values of either the experimental results or the theoretically predicted results from second-order perturbation theory. These discrepancies reinforce expectations that the soft-photon approximation is inaccurate for relatively low-energy ATI photoelectrons. Interestingly, the experimentally measured two-photon ATI anisotropy parameters have intermediate values between the theoretically predicted results from second-order perturbation theory and the soft-photon approximation for all sidebands except for the lowest-energy negative sideband of the 13th high-order harmonic.

The cross section ratios can be theoretically predicted using the soft-photon approximation in the low-intensity limit by integrating the expressions for the differential cross sections in eq 4 over all angles, resulting in an expression for the cross section ratio between the positive and negative two-photon ATI sidebands given by

$$\frac{\sigma^{(+)}}{\sigma^{(-)}} = \frac{k^{(+)}[\sigma^{(0)}(5 + 2\beta_2^{(0)})]_{E_{k(+)}}}{k^{(-)}[\sigma^{(0)}(5 + 2\beta_2^{(0)})]_{E_{k(-)}}} \qquad (5)$$

where $\sigma^{(0)}$ and $\beta_2^{(0)}$ are the single-photon ionization cross section and anisotropy parameter, respectively, evaluated at the photoelectron energy $E_{k(\pm)}$ of wave vector $k^{(\pm)}$ corresponding to the positive and negative two-photon ATI sidebands, respectively. Using experimentally measured SPI cross sections[28] from argon of 37.6, 37.0, and 34.9 Mb at the photon energies of 18.6, 21.7, and 24.9 eV, corresponding to the required energies for the ATI sidebands of interest, the cross section ratios between the positive and negative sidebands of the 13th and 15th high-order harmonics are theoretically determined to be 1.78 and 1.27, respectively. These values are listed in Table 1. Although the theoretically predicted cross section ratio using the soft-photon approximation for the 15th HH ATI sidebands is in agreement with experimental measurements, the corresponding result for the lower-energy 13th HH sideband does not agree with either the experimental measurements or theoretical predictions using second-order perturbation theory. The discrepancy between the soft-photon approximation and experimental results is not surprising considering that the model is only valid when the ATI sideband photoelectron energies are much higher than the photon energy of the dressing field.

The experimentally measured photoelectron angular distributions and cross section ratios of the positive and negative ATI sidebands allow for a fundamental test of two different theoretical treatments of two-photon above threshold ionization of the 3*p* electron of argon. Using second-order perturbation theory with a one-electron model generates excellent predictions for the cross section ratios between the positive and negative sidebands from the 13th HH + 800 nm and the 15th HH + 800 nm, but this level of theory does not reproduce experimental measurements of the anisotropy parameters. Using the soft-photon approximation allows an accurate prediction for only the cross section ratio associated with the higher-energy 15th HH ATI sidebands. Neither of the theories mutually agree with each other or with experimental results regarding the photoelectron angular distributions. The second-order perturbation theory deviations are attributed to a breakdown of the one-electron model from electron−electron correlations and from a final potential that is not spherically symmetric. In addition, the model potential used for the theoretical predictions neglects spin−orbit coupling. The soft-photon approximation inaccuracies are expected because the electron kinetic energies are comparable to the photon energy of the dressing field. In general, more sophisticated theoretical treatments are needed to correctly address the photoelectron angular distributions of two-color two-photon above threshold ionization of the 3*p* electron of argon.

Conclusion

In conclusion, the cross section ratios and anisotropy parameters from two-color two-photon above threshold ionization of argon with the selected 13th and 15th high-order harmonics in a perturbative 800 nm dressing field are measured using photoelectron velocity map imaging. A new method of data analysis based on anisotropy averaging and partial background subtraction is developed to accurately determine photoelectron angular distributions when an ATI signal energetically overlaps with a depleted single-photon ionization background. The experimentally measured cross section ratios between the positive and negative sidebands are in good agreement with theoretical predictions that use second-order perturbation theory and a one-electron model, but are only partly in agreement with results using the soft-photon approximation. Photoelectron angular distributions, which result from detailed interactions between the two photons, the atom, and the outgoing photoelectron, are a more sensitive test for fundamental models of two-photon ionization than angularly integrated cross sections. Deviations between the experimentally determined and theoretically derived anisotropy parameters demonstrate the need for a more comprehensive description of two-photon above threshold ionization processes.

Acknowledgment. The authors thank Daniel Strasser and Frédéric Fournier for their helpful discussions. The authors gratefully acknowledge financial support by the Director, Office of Science, Office of Basic Energy Sciences, Chemical Sciences, Geosciences, and Biosciences Division, U.S. Department of Energy under Contract No. DE-AC02-05CH11231. The authors are also grateful for related support for high-order harmonic generation studies from the National Science Foundation Engineering Research Center, Extreme Ultraviolet Science and Technology, EEC-0310717. Stephen Leone gratefully acknowledges the generous support of a Morris Belkin Visiting Professorship at the Weizmann Institute of Science. Stephen Leone also gratefully acknowledges the constant support and friendship of Bob Field throughout our entire careers.

Note Added after ASAP Publication. This Article was published on Articles ASAP on July 17, 2009. Corrections were made in the text after eq 3 (paragraph beginning "Deviations between...") and in the text three lines below eq 5. The corrected version was posted on August 3, 2009.

References and Notes

(1) Agostini, P.; DiMauro, L. F. *Rep. Prog. Phys.* **2004**, *67*, 813.
(2) DiMauro, L. F.; Agostini, P. *Adv. At., Mol., Opt. Phys.* **1995**, *35*, 79.
(3) Becker, W.; Grasbon, F.; Kopold, K.; Milošević, D. B.; Pauling, G. G.; Walther, H. *Adv. At., Mol., Opt. Phys.* **2002**, *48*, 35.
(4) Aseyev, S. A.; Ni, Y.; Frasinski, L. J.; Muller, H. G.; Vrakking, M. J. J. *Phys. Rev. Lett.* **2003**, *91*, 223902.
(5) Guyétand, O.; Gisselbrecht, M.; Huetz, A.; Agostini, P.; Taïeb, R.; Véniard, V.; Maquet, A.; Antonucci, L.; Boyko, O.; Valentin, C.; Douillet, D. *J. Phys. B* **2005**, *38*, L357.
(6) Guyétand, O.; Gisselbrecht, M.; Huetz, A.; Agostini, P.; Taïeb, R.; Maquet, A.; Carré, B.; Breger, P.; Gobert, O.; Garzella, D.; Hergott, J.-F.; Tcherbakoff, O.; Merdji, H.; Bougeard, M.; Rottke, H.; Böttcher, M.; Ansari, Z.; Antoine, P. *J. Phys. B* **2008**, *41*, 051002.
(7) Varjú, K.; Johnsson, P.; Mauritsson, J.; Remetter, T.; Ruchon, T.; Ni, Y.; Lépine, F.; Kling, M.; Khan, J.; Schafer, K. J.; Vrakking, M. J. J.; L'Huillier, A. *J. Phys. B* **2006**, *39*, 3983.
(8) O'Keefe, P.; López-Martens, R.; Mauritsson, J.; Johanson, A.; Huillier, A. L.; Véniard, V.; Taïeb, R.; Maquet, A.; Meyer, M. *Phys. Rev. A* **2004**, *69*, 051401.
(9) Meyer, M.; Cubaynes, D.; Glijer, D.; Dardis, J; Hayden, P; Hough, P; Richardson, V; Kennedy, E. T; Costello, J. T; Radcliffe, P; Düsterer, S.; Azima, A.; Li, W. B.; Redlin, H; Feldhaus, J; Taïeb, R; Maquet, A; Grum-Grzhimailo, A. N.; Gryzlova, E. V.; Strakhova, S. I. *Phys. Rev. Lett.* **2008**, *101*, 193002.
(10) Cionga, A.; Florescu, V.; Maquet, A.; Taïeb, R. *Phys. Rev. A* **1993**, *47*, 1830.
(11) Reid, K. L. *Annu. Rev. Phys. Chem.* **2003**, *54*, 397.
(12) Haber, L. H.; Doughty, B.; Leone, S. R. *Phys Rev. A* **2009**, *79*, 031401.
(13) Smith, S. J.; Leuchs, G. *Adv. Atom. Mol. Phys.* **1988**, *24*, 157.
(14) Chien, R.-L.; Mullins, O. C.; Berry, R. S. *Phys. Rev. A* **1983**, *28*, 2078.
(15) Reichle, R.; Helm, H.; Kiyan, I. Y. *Phys. Rev. A* **2003**, *68*, 063404.
(16) Schohl, S.; Cherepkov, N. A.; Petrov, I. D.; Sukhorukov, V. L.; Baier, S.; Hotop, H. *J. Phys. B* **1998**, *31*, 3363.
(17) Wang, Z.-M.; Elliot, D. S. *Phys. Rev. A* **2000**, *62*, 053404.
(18) Toma, E. S.; Muller, H. G. *J. Phys. B* **2002**, *35*, 3435.
(19) Cooper, J.; Zare, R. N. *Lect. Theor. Phys.* **1968**, *11C*, 317.
(20) Manson, S. T.; Cooper, J. W. *Phys. Rev.* **1968**, *165*, 126.
(21) Maquet, A.; Taïeb, R. *J. Mod. Opt.* **2007**, *54*, 1847.
(22) Kroll, N. M.; Watson, K. M. *Phys. Rev. A* **1973**, *8*, 804.
(23) Eppink, A. T. J. B.; Parker, D. H. *Rev. Sci. Instrum.* **1997**, *68*, 3477.
(24) Mairesse, Y.; Quéré, F. *Phys. Rev. A* **2005**, *71*, 011401.
(25) Garcia, G. A.; Nahon, L.; Powis, I. *Rev. Sci. Instrum.* **2004**, *75*, 4989.
(26) Taylor, K. T. *J. Phys. B* **1977**, *10*, L699.
(27) Houlgate, R. G.; West, J. B.; Codling, K.; Marr, G. V. *J. Electron Spectrosc.* **1976**, *9*, 205.
(28) Henke, B. L.; Gullikson, E. M.; Davis, J. C. *At. Data Nucl. Data* **1993**, *54*, 181 Current values are updated at http://www-cxro.lbl.gov/.

JP903231N